



HORIZON 2020

HORIZON 2020 RESEARCH AND INNOVATION FRAMEWORK PROGRAMME OF THE EUROPEAN ATOMIC ENERGY COMMUNITY

Nuclear Fission and Radiation Protection 2018 (NFRP-2018-4)

Project acronym: **SANDA**

Workpackages: **WP1**

Identification N°: **D1.1**

Type of document: Deliverable

Title of deliverable: Report on the study and construction of new devices for precise fission cross section measurements

Dissemination Level: **PU**

| | Name | Partner | Date | Signature |
|------------------|-------------|---------|------------|---|
| Prepared by: | L .Mathieu | 5 | 29-02-2024 |  |
| WP leader: | M. Kerveno | 5 | 07-03-2024 |  |
| IP Co-ordinator: | E. González | 1 | | |

Part I: Development of the Gaseous Proton Recoil Telescope for neutron flux measurement

L. Mathieu*, M. Aïche, S. Czajkowski, P. Marini, I. Tsekhanovich
LP2I Bordeaux, UMR5797, Université de Bordeaux, CNRS, F-33170, Gradignan, France
*e-mail : mathieu@lp2i.in2p3.fr

February 26, 2024

1 Introduction

One of the primary difficulties in determining neutron-induced fission cross sections lies in accurately measuring the neutron flux. Usually, reactions such as $^{235}\text{U}(n,f)$ or $^{238}\text{U}(n,f)$ are employed to normalize the measured fission rate [1-4]. For these two reactions, the discrepancies between evaluations and/or with existing data are up to 4% and 10% respectively in the MeV neutron energy range. In such experiment, the reference sample is positioned alongside the sample(s) under investigation, subject to the same experimental conditions. This creates a significant correlation between the cross section being studied and the standard one. In addition, the reference measurement often uses the same physical detection process (detection of fission fragments) and may therefore share systematic uncertainties, which further increases correlations.

The elastic $^1\text{H}(n,p)$ reaction is another standard reaction, known with an accuracy of 0.2% in the MeV energy range. Its detection process is also completely different from the usual reference measurements, increasing the independence of the obtained result. It has been used in the past by our research team to measure fission cross section with very good accuracy for neutron energies above 1 MeV [5,6].

To perform such experiment, recoil protons are produced by a few μm -thick H-rich collimated foil, and detected by a collimated $50\mu\text{m}$ -thick Si detector positioned few centimetres downstream. Only recoil protons emitted close to 0° , with energies close to the initial neutron energy, are detected as a peak in the detected proton spectrum. The background is measured by masking the H-rich foil and subtracting it from the proton spectrum. With a low background contribution, the subtraction process is effective: the proton peak can be integrated accurately, with a low dependency on the integration limits (see left part of Figure 1).

2 Challenge for neutron energies below 1 MeV

In [6], it has been observed a very high background contribution in the detected proton spectrum below 1 MeV (see right part of Figure 1). However, the accuracy reduction for the neutron energies of interest (above 1 MeV) was still acceptable.

A test experiment was performed in 2015 at the AIFIRA facility in Bordeaux, to investigate this background. Various neutron energies were used, and spectra of recoil protons were recorded. The background subtraction process is never ideal and a high background remains at low energy after subtraction. For proton peak at energies below 1 MeV (see Figure 2), it completely prevents accurate measurement of neutron flux [7].

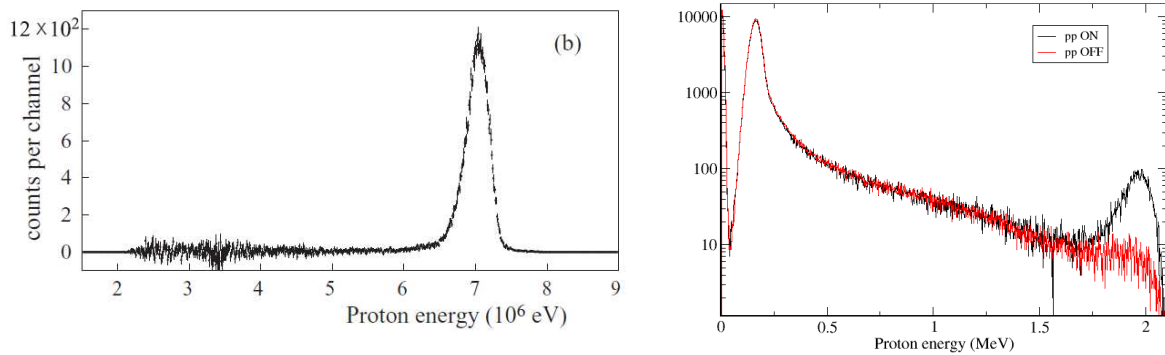


Figure 1: (left) Proton spectrum for high neutron energy (7 MeV) after background subtraction. The recoil proton peak is well defined, with a very low low-energy tail. (right) Proton spectrum for lower neutron energy (2 MeV) for flux and background measurement.

Test carried out during this experiment, in addition to the MCNP simulations, shed light on the origin of the problem. A large number of γ -rays are produced by the neutron capture process in the beam dump and surrounding materials. These γ -rays generates an intense electron flux going through every part of the experimental setup (see left part of Figure 3) [7].

Electrons deposit much less energy in matter than recoil protons due to their lower stopping power. Nevertheless, an electron of few 100 keV deposits its energy in the whole thickness of a Silicon detector (here 50 μm), whereas a protons of 700 keV or 200 keV in the same detector has a range of 10 μm and 2 μm respectively. In addition, simulations show that many electrons reach the Si detector with a high incident angles, further increasing the effective thickness and thus the energy deposition. Finally, the high electron flux induces pile-up events in the Si detector, contributing to the exponential-shaped high-energy part of the background (see right part of Figure 3).

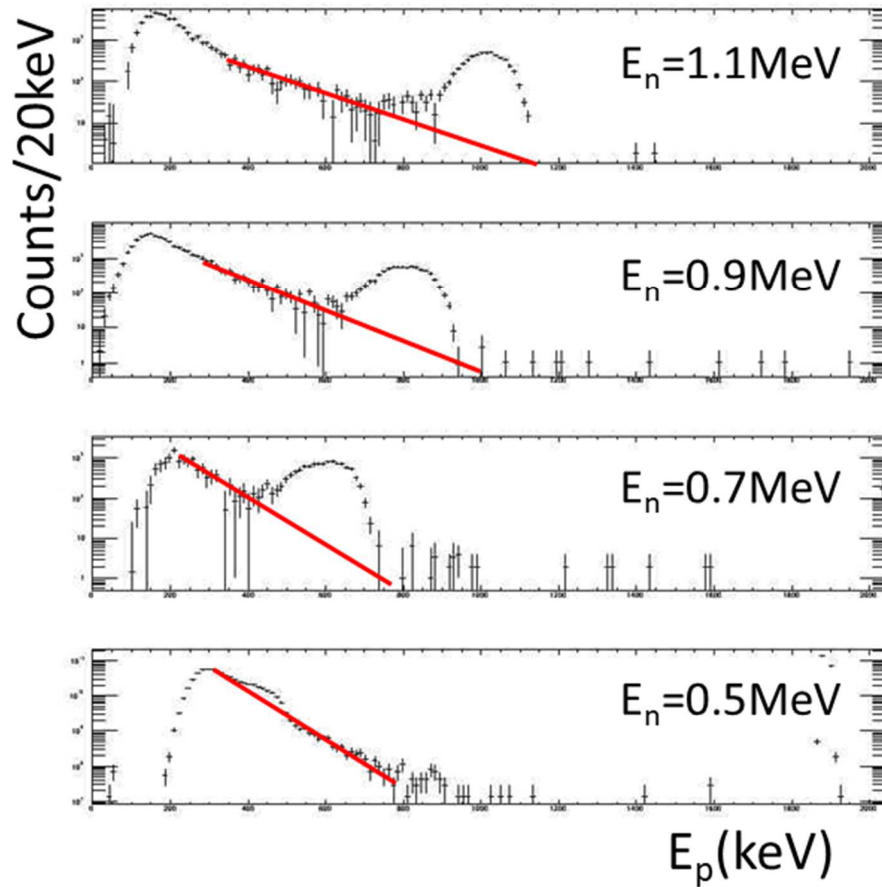


Figure 2: Proton spectrum after background subtraction for different neutron energies. Below 1 MeV, the background contribution is still very high, preventing an accurate determination of the number of recoil protons.

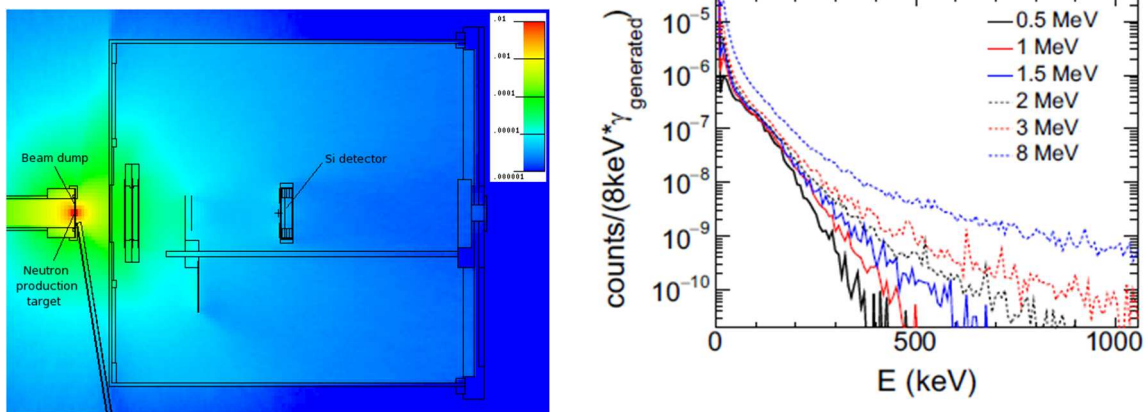


Figure 3: (left) MCNP simulation of the electron flux expressed in part/cm² for one source particle. The electrons are generated by a 1MeV γ -ray source located at the neutron production target. (right) Detected spectrum in the Si detector for electrons generated, depending on the electron initial energy.

3 Gaseous Proton Recoil Telescope (GPRT) detector

As part of the CHANDA project, a prototype detector has been designed and built. This detector has a number of features designed to meet the challenge of measuring recoil protons in an environment dense with γ -rays and electrons.

The detector principle is based on the energy deposition in a gas. The gas was first CF_4 , for its higher electron drift velocity, but a slower gas mixture $\text{N}_2\text{-CO}_2$ (70/30) was finally chosen. The gas pressure can be adapted in order that the proton range is comparable to the detector length. By doing this, electrons cannot deposit a lot of energy in the detector, since there is not enough material thickness for that. It gives the detector a low sensitivity to e^-/γ -rays.

The detector dimensions are $4 \times 4 \times 12 \text{ cm}^3$, and a H-rich foil (radiator) is placed at the entrance of the detector. Recoiling protons ionise the gas and primary electrons then drift toward the anode. To adapt the radiator thickness to the neutron energy, several H-rich foils are placed on a rotating disk (see Figure 4). A step-by-step motor remotely-controlled enables the selection of the proper foil. For neutron flux measurement applications, precise knowledge of the detection efficiency is mandatory. A collimator is therefore positioned inside the detector (splitting the detector into two ionisation chambers ΔE and E), in order to select only the recoil protons emitted at forward angle.

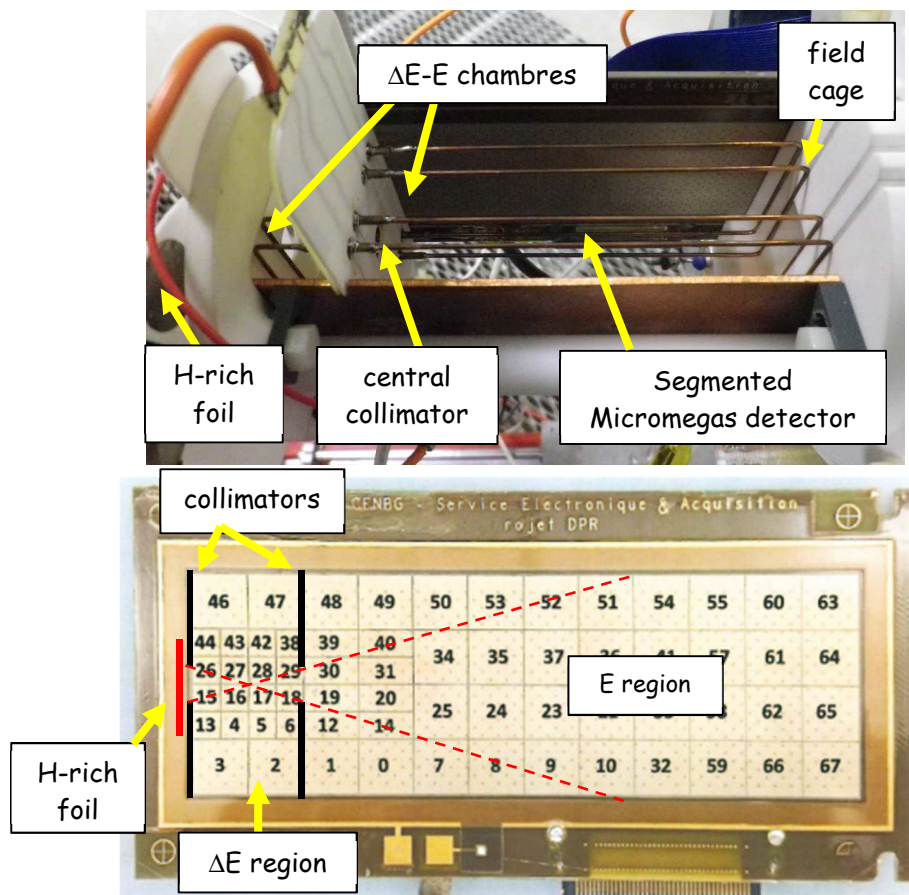


Figure 4: (upper part) Picture of GPRT. (lower part) Picture of the Micromegas segmented detection plane, with pad and item labels and collimator positions.

In order to amplify the signal given by gas ionisation, the detector relies on micromegas technology [8]: a grid is placed 125 μm above the anode and polarized. The high electric field, of about 40 kV/cm in this region induces electron multiplication and signal amplification.

In addition to a low sensitivity to background γ -rays/ e^- , the detector should be able to reject background recoil proton events, induced by scattered neutrons on the radiator, or by direct neutrons on other surrounding materials. These protons can be discriminated by a track analysis. The detection plane is therefore segmented in 64 pads, with a smaller segmentation at the entrance. To avoid (or greatly reduce) any contaminant proton recoil from structure materials, many pieces were made in ceramic (Macor).

To have a uniform electric field between the electrodes, a field cage has been added. To reduce the amount of materials in the GPRT, the field cage is self-supporting (thick wires) and attached to the collimator. The bias is distributed to each wire via the cathode potential, a series of electrical resistors and a variable resistor (to adapt to the grid potential which depends on the gas pressure).

At the end of the CHANDA project and the beginning of the SANDA project, general performances of the GPRT were satisfactory:

- proton track can be reconstructed
- the detector has a very low sensitivity to γ -rays/ e^- : a test without H-rich foil gives no signal, because each pad is not sensitive enough to see signal from background electrons
- direct neutrons can be discriminated from scattered neutrons (based on their energy and so track length)
- low detection energy limit at 200 keV neutron energy has been achieved
- no pile-up was observed : due to the low counting rate of the recoil protons, and the very low sensitivity to background events, no pile-up have been observed.
- the slow N_2 - CO_2 enables to measure the electron drift time, giving access to the third dimension of the proton track
- general functioning of electronics, acquisition system, gas regulation, rotating disk control...

Despite the general functioning of the GPRT, it appears the proton energy will not be determined by summing the energy deposited on every pad. To do that, one has to be sure that (i) primary electrons are totally collected (no loss), (ii) every pad has the exact same gain. The first point is not true, because the GPRT collimator induce a strong electric field disturbance. Corrective actions have been applied, but electric field in the ΔE chamber and close to the collimator is not uniform. This is why the proton energy will rely on the track length rather than its energy deposition. For this purpose, it is mandatory to have access to the 3D track.

The key point which was not achieved at the beginning of the SANDA project concerned the detection efficiency. For a neutron flux detector, an intrinsic efficiency of 100% is mandatory, to be sure no event is lost in the process. Several hints suggested a poor intrinsic efficiency, but no quantitative experiment had been carried out so far.

4 Efficiency experiments (and other tests) in irradiation chamber

The first test performed was to investigate this issue with an alpha source. The source activity was measured in a dedicated experiment within 1% of uncertainty. The alpha source was placed at the entrance of the GPRT and alpha tracks were recorded, at a rate of approximately 4.5 alpha/s since most of the alpha do not go through the central collimator.

Taking into account systematic uncertainties due to source activity, source positioning and distance measurement, the measured intrinsic efficiency was $(99.2 \pm 3.7^{sys})\%$. This results was encouraging, since it was compatible with 100%, but it was not accurate enough to validate the GPRT as a neutron flux detector.

Considering the alpha source method limits, a dedicated experiment was designed (see Figure 5). The goal was to send a proton micro-beam from the AIFIRA facility directly into the GPRT detector. A Si detector placed downstream the GPRT was used to count the number of protons sent. The GPRT intrinsic efficiency is then given by the detection ratio between these two detectors.

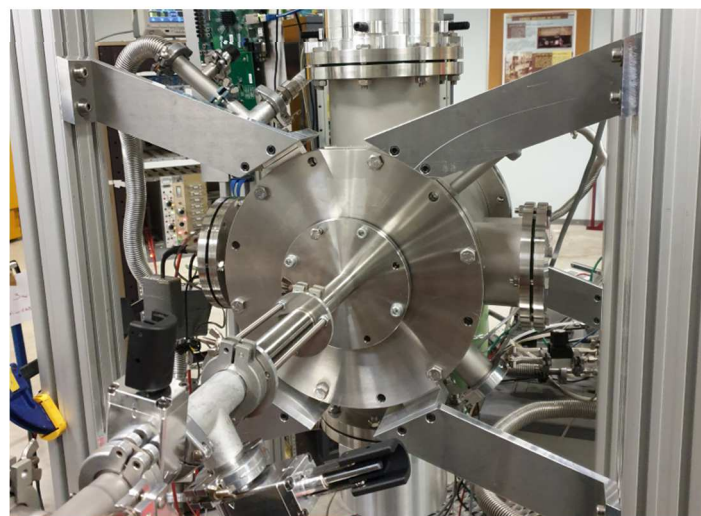
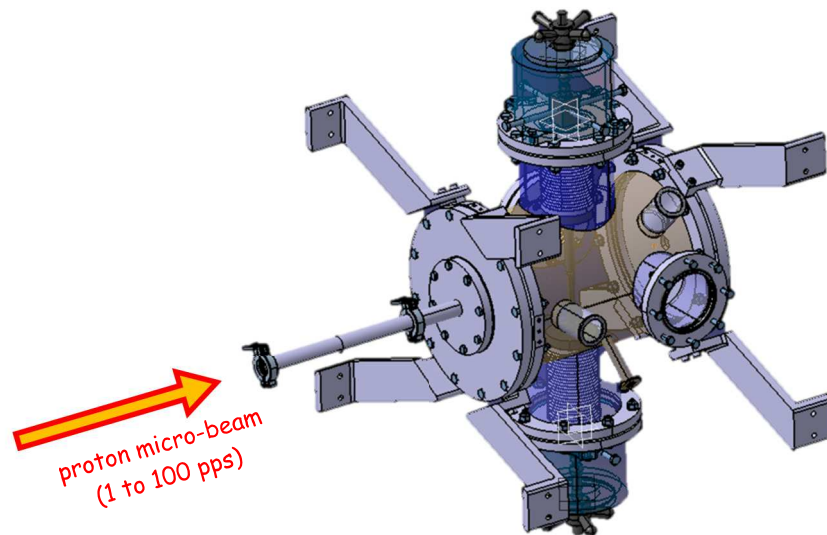


Figure 5: (up) Scheme and (low) picture of the dedicated irradiation chamber. The chamber is connected to the accelerator pipe, and several collimators are used to make the micro-beam and send it into the GPRT.

To mimic the conditions of a real proton-recoil experiment, the beam intensity has to be very low, between 1 to 100 particles per second, and protons must pass through the GPRT and be detected in the Si downstream. To achieve such a level of performance, experience has led to the use of three collimators:

- a 20 μm collimator: this reduce considerably the beam intensity by allowing only a small part to pass through. With a input beam of approximately 1 nA, it enabled us to achieve a level of a few particles per second.
- a 2 mm pre-collimator: this insulated collimator helps the accelerator operator to centre the beam and reach the main collimator (with current reading)
- a 2mm post-collimator: the main collimator and the thin window (separating accelerator vacuum from GPRT gas chamber) can scatters protons. These protons will go through the GPRT with an angle, and will not reach the Si detector downstream. This post-collimator at the entrance of the GPRT selects only protons going straight ahead.

Results showed an abnormal behaviour: the intrinsic efficiency was 100% for low counting rates (below few pps), but dropped to 30% at 30 pps, and even 10% at 100 pps. This result was compatible with the alpha experiment performed at low counting rate, but the drop at high counting rate was a critical flaw.

Apart from efficiency measurements, some other tests have been performed to take benefit of the very clean experimental conditions: no n, γ or e^- production (low noise), precise initial energy, precise initial position, and precise direction (straight ahead). These tests were useful to better characterise the detector behaviour.

First, proton micro-beam has been sent through the GPRT from different entry points, in steps of 0.5 mm. As the proton only goes straight ahead, primary electrons generated activate only one line of pads. When the beam enter the GPRT in between the electrodes, primary electrons have to drift 2 cm to reach the grid. This drift may cause lateral diffusion and decrease the spatial resolution. It has been tested that from one entry point to the other 0.5 mm away, the pad activation completely switched from one line to the other. This proves that the drift lateral spread is less than 0.25mm for a 2 cm drift, which is more than enough for our foreseen applications.

The beam was sent in different parts of the GPRT to test the electric field uniformity inside the field cage. An electric field non-uniformity appears as a decrease in signal amplitude due to the loss of some primary electrons. Such phenomenon had been observed with alpha source in standard chamber for the last few centimetres of the GPRT. This was due to the bottom of the chamber, electrically connected to the ground, which was too close to the GPRT rear part. In the irradiation chamber, with a completely different configuration, this phenomenon was not seen. Only a slight field non-uniformity has been revealed on few millimetres on the side of the GPRT. This confirms that the last few centimetres of the GPRT should not be used to exploit traces quantitatively, until the problem with the chambers bottom has been solved.

The electron drift toward the grid may also induce a loss of amplitude, via electron recombination in the gas. Proton beam was sent at different entry points, inducing different drift lengths (close to the grid, or close to the cathode). No difference in amplitude has been observed with the gas mixture used. This feature is important for track reconstruction.

With precise energy and direction in a clean environment, proton tracks are much easier to analyse than recoil proton tracks from neutrons irradiation, or alpha tracks from a multi alpha source. Different bias were tested in order to follow the change in signal amplitude. The experimental gain was calculated and compared to theoretical calculations.

5 Digital Acquisition system

The detector output consists in 64 channels corresponding to the 64 pads. This output is read by a dedicated electronic. The system used is derived from the GET electronics developed at CEA in the 2010's for TPC chambers. This electronic was adapted by the LP2i electronic department to use a single 64-channel module, and then called SAM (Single AGET Module). This DAQ allows users to select which channel and how many of them participate to the event trigger. It defines thresholds and amplitude ranges. One event represents 64 channel with 512 values (sampled every 10 ns).

It appeared very early that the SAM electronics was still in development. Various issues has been solved over the years, such as the fact that every second event was missing (issue discovered during the experiment with the calibrated alpha source). After having checked the detector behaviour in various conditions, it appeared that the DAQ was again responsible for the lack of efficiency.

This led to issues in the project advancement, since this project is only a small project of the LP2i electronics department, for instance much smaller than electronics modules fabrication for JUNO giant experiment. This incurred considerable delays.

Nevertheless, investigations were carried out on signal transmission, and critical steps were taken in 2023. One of the main issue was the fluctuating loss of events between the DAQ and the computer. Indeed, tests on bench with a periodic pulser were not able to properly describe the system dead time. Instead of a 100% \rightarrow 50% sharp transition at a critical frequency, the efficiency smoothly decreased. It also depended on external parameters like PC or DAQ reboot. It appeared that the DAQ buffer feature was not working properly. By disabling this buffer, in a "1 event \rightarrow 1 transmission" degraded mode, the system no longer loses any events. A test has been performed with the GPRT and an external trigger (to monitor the figures), and nearly 100% of the events were recorded, despite the high counting rate (several 10 trigger/sec).

The microscopic dead time is measured to be 7.3 ms. It is far superior to the theoretical 1.3 ms taken to read the detectors data (64 channels x 512 values / 25 MHz). The remaining 6 ms are due to the data transfer.

It is important that the dead time correction remains low in order to maintain a small uncertainty in the neutron flux measured. At a rate of 10 proton/sec, 7% of them would be lost because of the dead time: 1% during the data reading, 6% during data transfer. Interestingly, the latter are

not registered but the DAQ still records the number of “missed” trigger. Then only the former is a real issue.

A DAQ function has also been fixed, allowing only channels with a signal to be recorded. It limits the number of channels to read and transfer by a factor of 2 to 4. Dead time is then be reduced accordingly.

6 Analysis tools

An accurate neutron flux measurement based on proton recoil technique requires a large number of detected protons to minimise statistical uncertainty. With the GPRT, at least 10 000 tracks would have to be analysed, which is impossible without an automated analysis tool. Moreover, the viewer currently used is based on the GET debug software, and is far from being user friendly.

Such automated analysis tool must have certain features:

- It must be able to remove parasitic frames. The DAQ is sometimes triggered by electromagnetic noise, and an event is recorded without any physical energy deposition. These frames may comprise many channels with chaotic signal amplitudes, or very large and saturated amplitudes affecting each channel. The automated analysis tool must be able to remove these frames properly, without leaving any or removing physical frames.
- Some electronic noises may distort the signal amplitude of a physical event. It can lead to incorrect amplitude reading, and affect the determination of the track length. The automated analysis tool must be able to correct as much as possible this phenomenon.
- Each channel as its own baseline. This has to be normalized in order to evaluate properly the signal amplitudes.
- The analysis tool must make it easy to navigate through the various frames and display the tracks (in 2D or even 3D if required). This is mandatory to manually check the code performances before validating it for automatic use.
- The code will have to estimate the real track length in 3D, by carefully fitting the end of the track (pads in E chamber are quite large). It will then implement a histogram to display the recoil proton peak.

Effort has been made in 2023 to develop this automatic tool, and a python code was implemented. This code allows to navigate through the frames (each channel is visible for a given frame) or through the channels (each frame is visible for a given channel). The former is useful to have access to given physical event, and the latter helps to identify quickly abnormal frames.

Figure 6 presents the frame of a physical event, before and after treatment by the automated code. Raw data shows baselines with different offsets, and a parasitic noise affecting a lot of channel simultaneously. The code renormalized baselines, and a correction was applied to the parasitic noise. Indeed, a statistical study of curves maxima enables to identify an “averaged noise” which can then be subtracted. This method is of particular importance when noise and physical signal are simultaneous.

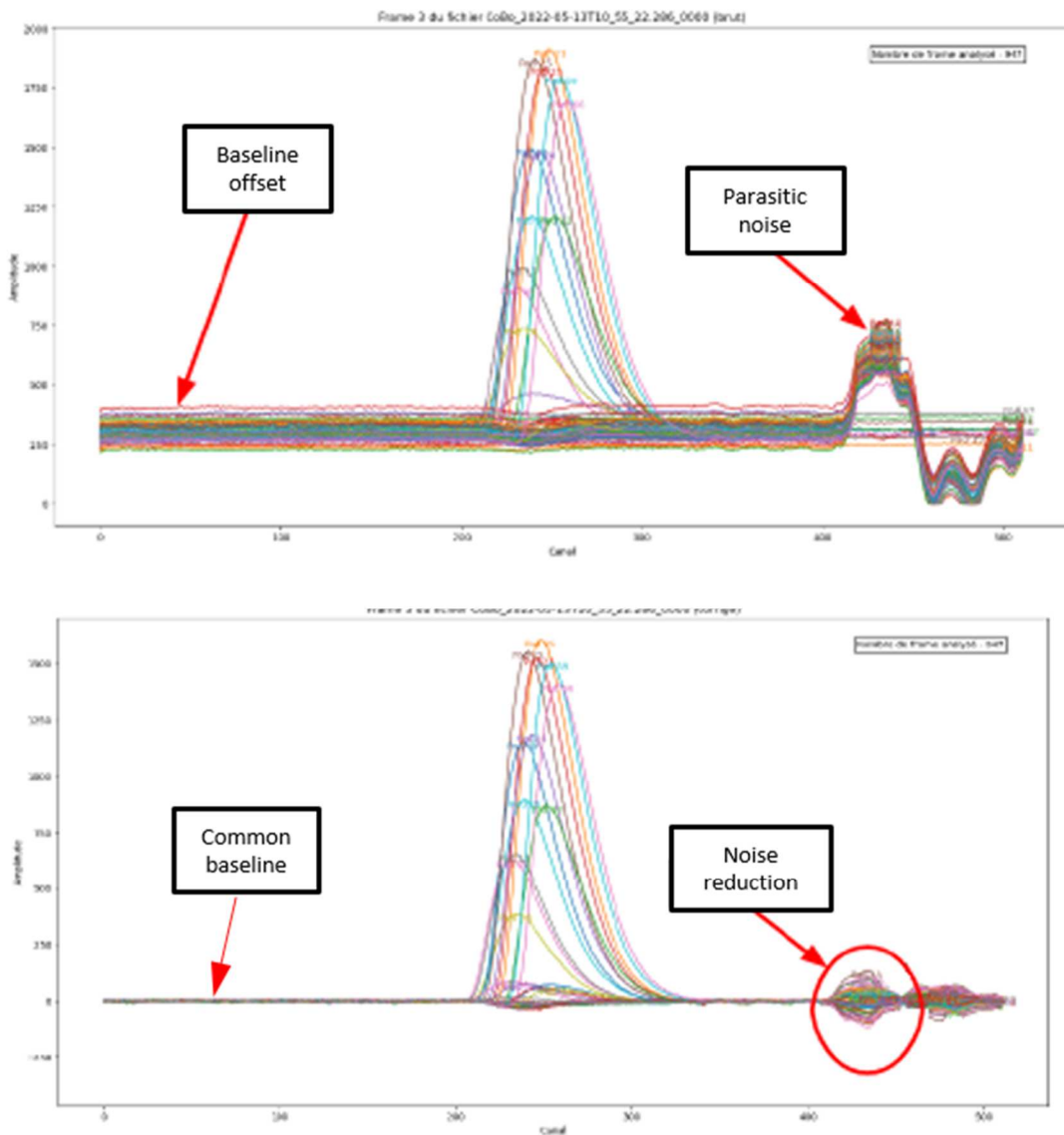


Figure 6: Signal amplitude for a physical event frame: (upper part) raw data, or (lower part) corrected data

The code can switch from standard display to 2D display back and forth. Figure 7 illustrates a 2D plot of an alpha track. This feature has still to be improved: all GPRT pads do not have the same size, which complicate plotting. For the moment, it is treated by dividing larger pads, as can be seen on the figure with channel 34 divided into 4 smaller matrix values.

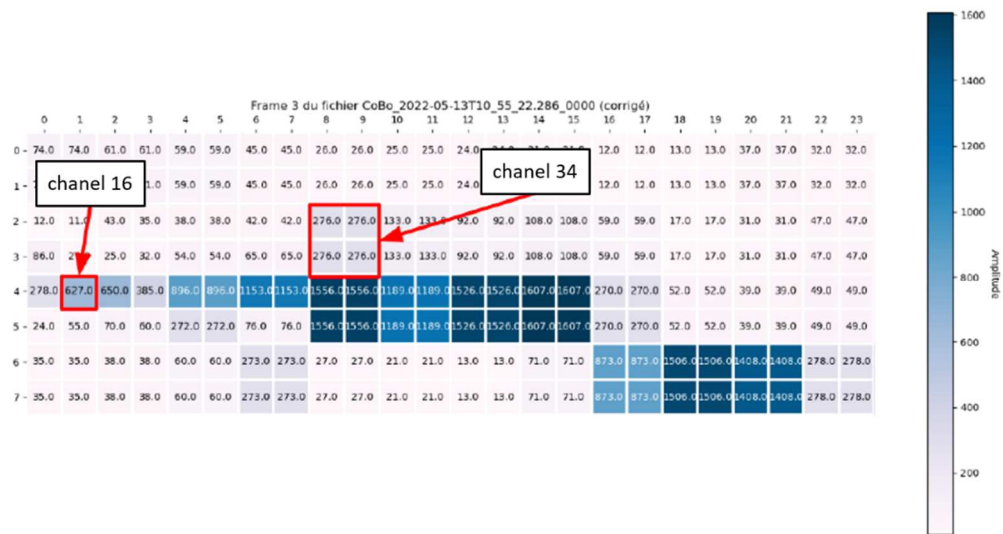


Figure 7: 2D plot of an alpha particle in the GPRC. Colours and numbers represent the energy deposited in each pad.

7 Conclusion

The Gaseous Proton Recoil Telescope began development as part of the CHANDA project. However, development was not yet complete: there were still serious doubts about its detection efficiency, and no automatic analysis programme existed.

Efforts focused on characterising detection efficiency, identifying the problem and correcting it. It appeared that the issue was with the transfer of data from the DAQ, during which information (events) was being lost. A corrective measure and a degraded operating mode now enables the system to operate with a much reduced and quantifiable loss of events (dead time). Improvements are still foreseen to further reduce the dead time.

At the same time, tests continued to characterise and improve the detector. They showed that the drift of the primary electrons did not lead to signal loss or spatial dispersion. This will be useful for reconstructing the track and determining the track length of the recoil protons.

Finally, an automated analysis code was written. Several essential functions have been implemented, such as data visualisation/navigation, and the ability to filter out the electromagnetic noise present in certain events. To be completed, this code requires an automatic event sorting function (so that only the recoil proton tracks are output), as well as an algorithm for determining the track length. Work on these aspects will continue over the coming months.

As a result, the GPRC now meets the minimum specifications to be used as neutron flux detector.

References

- [1] C. Paradela, The n_TOF collaboration, Phys. Rev. C 82, (2010) 034601
- [2] A. Tsinganis, The n_TOF collaboration, Nucl. Data Sheets 119, 58 (2014)
- [3] P. Salvador-Castiñeira, T. Brys, R. Eykens, F.-J. Hamsch, A. Göök, A. Moens, S. Oberstedt, G. Sibbens, D. Vanleeuw, M. Vidali, C. Pretel, Phys. Rev. C 92 (2015) 044606.
- [4] C. Matei, F. Belloni, J. Heyse, A.J.M Plompen, D.J. Thomas, Phys. Rev. C 95 (2017) 024606.
- [5] G. Kessedjian, G. Barreau, M. Aïche, B. Jurado, A. Bidaud, S. Czajkowski, D. Dassié, B. Haas, L. Mathieu, L. Tassan-Got et al., Phys. Rev. C 85, 044613 (2012)
- [6] P. Marini, L. Mathieu, M. Aïche, G. Belier, S. Czajkowski, Q. Ducasse, B. Jurado, G. Kessedjian, J. Matarranz, A. Plompen, P. Salvador-Castiñeira, J. Taieb, and I. Tsekhanovich, Phys. Rev. C 96, 054604 (2017).
- [7] P. Marini, L. Mathieu, L. Acosta, M. Aïche, S. Czajkowski, B. Jurado, I. Tsekhanovich, Nucl. Instr. and Meth. A 841 (2017) 56-64
- [8] Y. Giomataris, Ph. Rebourgeard, J.P. Robert, G. Charpak, Nucl. Instr and Meth. A 376, 29 (1996)

Part II: Simulations for an XY Micromegas detector

G. Tsiledakis*, E. Berthoumieux, E. Dupont, F. Gunsing, G. Kaur
CEA Irfu, University Paris-Saclay, F-91191 Gif-sur-Yvette, France
*email: georgios.tsiledakis@cea.fr

February 23, 2024

1 Context

This project is part of deliverable D1.1 (*Report on the study and construction of new devices for precise fission cross section measurements*) of the SANDA project and includes the developments on Monte Carlo simulations related to an XY-neutron beam detector based on Micromegas technology. The detector will exploit coincident strip timing which will allow for the reconstitution of particle tracks in time projection chamber mode. Dedicated VMM3-chip electronics will be used for the data acquisition compatible with neutron time of flight measurements. The detector can be used to measure as a function of neutron-energy the spatial beam profile, (n,f) or (n,lcp) cross sections, or the angular distribution of neutron-induced fission fragments and light charged particles (lcp). The relative "transparency" for neutrons allows for the stacking of similar detectors or for an experimental setup, in particular a neutron capture measurement, downstream of the detector. A neutron capture setup in conjunction with an energy-dependent beam profile would narrow down the capture cross section uncertainties related to an energy-dependent normalization. The present reporting will focus on the simulations part of the project, as intended with the initial commitment for this deliverable. The hardware part of the project has been funded by the French national funding agency ANR.

2 Micromegas XY-strip "transparent" neutron detector

Micromegas detectors are used in a multitude of physics projects, as part of large high-energy physics detectors, but also in low-energy nuclear physics, including neutron-beam related detectors. The detector we are developing is intended to have a very low interaction with neutrons ("transparent") by limiting the in-beam materials to a minimum. The flexibility in gain of Micromegas detectors by a change of the high voltage allows to focus the detection either to light charged particles from neutron-induced reactions, or to the heavier fission fragments, depending on the neutron-conversion layer integrated in the detector. The principle of a Micromegas as a neutron detector within this project is schematically shown in figure 1. The incoming neutron beam is converted to a charged particle, typically a proton, alpha, or fission fragment, at the drift cathode and subsequently detected by the mesh-anode ensemble which is the actual detector.

Measurements with a beam profile [1, 2, 3] or TPC configuration of the detector will eventually

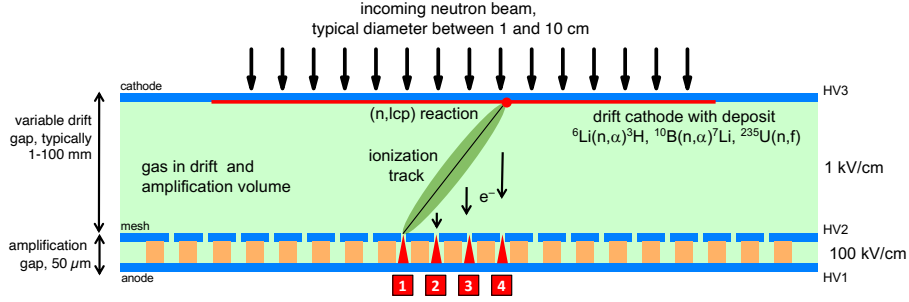


Figure 1. The principle of the microbulk Micromegas detector as a neutron detector. The neutron beam has a diameter of several cm, depending on the used collimators. The drift electrode is coated with a thin layer of material creating charged particles by neutron-induced reactions. The resulting charged particle ionizes the gas in the drift region. The electrons are multiplied in the amplification region consisting of a copper-coated kapton foil on which the micro-mesh pattern is applied. The fast signal is usually read out at either the mesh or the anode and multiple read-outs are realized with multiple strips.

result in a primary stream of events consisting of strip number, time, and amplitude which are the input quantities for the post-processing procedure. After coincidence analysis and cluster identification, the primary events will be transformed into events consisting of time-of-flight (neutron energy), the X and Y position of the neutron interaction point, and the angle of the particle track. In this step the constraint of searching for a single or at maximum two rectilinear tracks, originating from the neutron drift plane, will help to discriminate against background events from proton recoils produced in the gas. The application as a time projection chamber will need further development of the tracking algorithms and will lead also to the investigation of angular distributions of fission fragments and light charged particles induced by neutron reactions.

The amplification stage (between mesh and anode) of the detector is only 50 μm . This is the actual detector produced as a Kapton foil, coated on both sides with a 5 μm copper layer and partly etched away in such a way to form pillars to separate the copper layers. The latest production techniques as developed at CERN allow to shape the copper layers on both sides as orthogonal strips, hence the name "XY" detector. In this region, the high electric field, in the order of 100 kV/cm, induces a fast avalanche process of the electrons and the gaseous detector operates in the proportional counter regime. The detector signal is read out on both sides of this amplification region. The signal is a measure of the number of electrons arriving at the mesh and is characteristic for the position and time of an electron track at the end of the drift region.

In the drift region (between cathode and mesh), the electric field is low, in the order of 1 kV/cm, resulting in the operation of the detector as an ionization chamber. The drift region is the variable part of the detector in the sense that the distance can be chosen as an adjustable variable, depending on the exact use of the detector. In the case of neutron applications, the drift distance is typically between 1 and 100 mm, depending on the application. The information of the ionization tracks of the neutron-induced charged particles and the electron deposits at the level of the mesh in the drift region are the critical elements needed to be fine-tuned to operate the detector for a specific use, for example as a time- projection chamber (TPC).

The goal of the current task of the deliverable is to set up a tool chain to extract this information using Monte Carlo simulations. Since the ionization tracks and produced electron showers

are processes which can take excessive computing time to follow each electron individually, compromises have to be made in the simulation setups. As will be explained in the following, we have used several simulation codes to obtain our results, including FLUKA [4, 5, 6], Geant4[7, 8], Garfield++ [9], and SRIM [10].

3 Simulations

In this section we describe in more detail the simulations concerning the neutron-induced charged particle production in the cathode, the energy loss and primary ionization of charged particles in the drift region, as well as the electron interactions during the transport in the electric field of the detector. Detailed Monte Carlo simulations have been performed to evaluate the expected energy deposition spectra and explain the experimental total amplitude histograms that could be obtained by using the "XY" micromegas detector for in-beam neutron measurements. A photo of the sensitive area of the current detector, tested and installed in our lab, is shown in figure 2 (left and middle picture). This prototype has an active area of $10 \times 10 \text{ cm}^2$ and a drift gap, used for the measurements in the lab as well as for the most of the simulations, of 1 cm. At the moment, many tests are in progress for the characterisation of the detector performance with low energy X-rays, using a ^{55}Fe source and a gas mixture of 95% argon–5% isobutane (iC_4H_{10}) at atmospheric pressure. The detector voltages were typically $V_{\text{drift}} = -600 \text{ V}$, $V_{\text{mesh}} = 0 \text{ V}$ and $V_{\text{pad}} = +350 \text{ V}$. A preliminary total amplitude distribution obtained from the anode strips, when a collimated ^{55}Fe source irradiates the central part of the detector, is shown in the right picture of figure 2. The dominant peak of the experimental spectrum comes from the ^{55}Fe source ($E_{K_\alpha} = 5.9 \text{ keV}$, $E_{K_\beta} = 6.5 \text{ keV}$), while the smaller peak on the left is the argon escape peak.

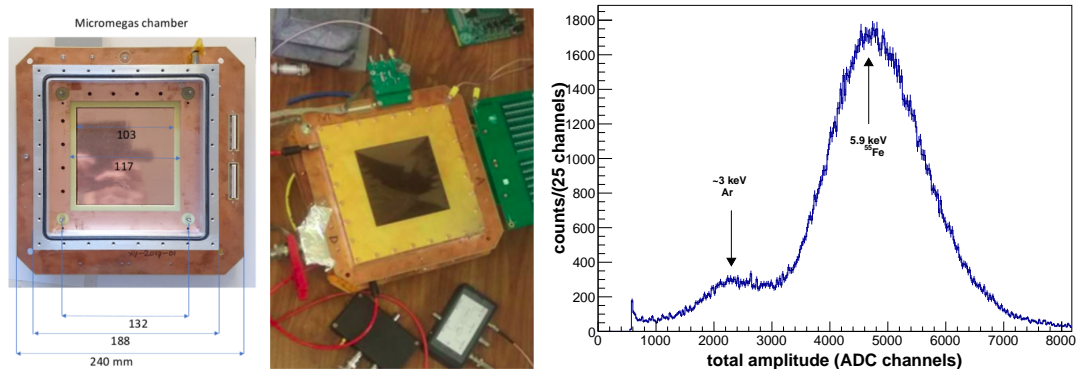


Figure 2. Current micromegas detector installed in the lab (left and middle picture) and preliminary tests providing an experimental total amplitude spectrum from the anode strips using a collimated ^{55}Fe source irradiating the central part of the detector (right picture).

Our first task was to simulate the response of the detector to thermal neutrons using the solid neutron-to-charge converters like ^6LiF , ^{10}B or $^{10}\text{B}_4\text{C}$ that are mounted inside the gas volume. The neutron converter used in this study was ^6Li , producing two ionizing particles, a triton and a ^4He particle via the well known $^6\text{Li}(n,t)^4\text{He}$ reaction that are emitted in opposite directions, with energies $E_t = 2.73 \text{ MeV}$ and $E_{^4\text{He}} = 2.05 \text{ MeV}$ respectively [11, 12]. For a given neutron interaction point the direction the two capture fragments are emitted is isotropically distributed. The detector response, depending on its geometry, will be different according to the particle ejection direction. A 9 cm diameter ^6LiF layer of $91.8 \mu\text{mg}/\text{cm}^2$ was deposited on a thin aluminised mylar backing (used as the drift electrode). In order to estimate the expected

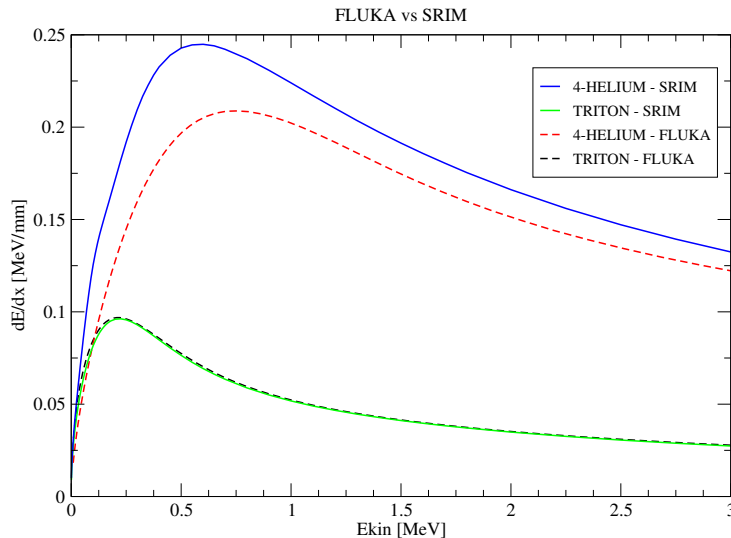


Figure 3. The stopping power (dE/dx) as a function of the kinetic energy of the ion as estimated by SRIM and FLUKA for a gas mixture of 95% argon–5% isobutane (iC_4H_{10}) at NTP conditions.

energy deposition of the alphas and the tritons in the gas and understand the experimental total amplitude histograms, detailed, comprehensive, and accurate Monte Carlo simulations needed to be performed. For the current work, the FLUKA Monte-Carlo simulation package was used (simulation results using the Geant4platform were compared to cross-validate the code), where the low energy neutron transport package was activated and employed for thermal neutron detection. The stopping power (dE/dx) of the alpha and triton particles as a function of their kinetic energy, is calculated with the FLUKA [4, 5] and SRIM [10] codes, as can be seen in figure 3. The discrepancy between FLUKA and SRIM observed for alpha particles seems actually to indicate an underestimation (attributed to a "different" stopping power recipe used in FLUKA). For this specific low-energy alpha case, one may indeed take IAEA data [13], with which the NIST table [14] is in line, as a reference that agrees with what SRIM provides. In the case of tritons, the results obtained by FLUKA and SRIM are in perfect agreement.

The range of a charged particle is the distance it travels before coming to rest (not equal to the energy divided by the total (electronic plus nuclear) stopping power). From this quantity one can deduce the electronic stopping power as a function of penetration depth (also known as the Bragg curve). This is shown in figure 4 for triton (in red) and α (in blue) particles from the ${}^6\text{Li}(n,\alpha)t$ reaction, and for two typical light, ${}^{95}\text{Sr}$ (in green), and heavy, ${}^{138}\text{Xe}$ (in black) fission fragments travelling in an Ar + 5% isobutane gas mixture at atmospheric pressure. A Bragg peak, close to the end of the track, is only clearly visible for triton and α particles. The range for a 2.73 MeV triton is about 6 cm, while α and fission fragments particles have a much smaller range due to their higher stopping power.

The geometry of the detector setup was implemented in detail, and a perpendicular point-like thermal neutron beam of 10M primaries was impinging on the centre of the ${}^6\text{LiF}$ target (0.35 μmm thick). The energy deposition of the alphas and the tritons was scored independently in the active gas volume of the detector. Monte Carlo simulation results are shown in figure 5,

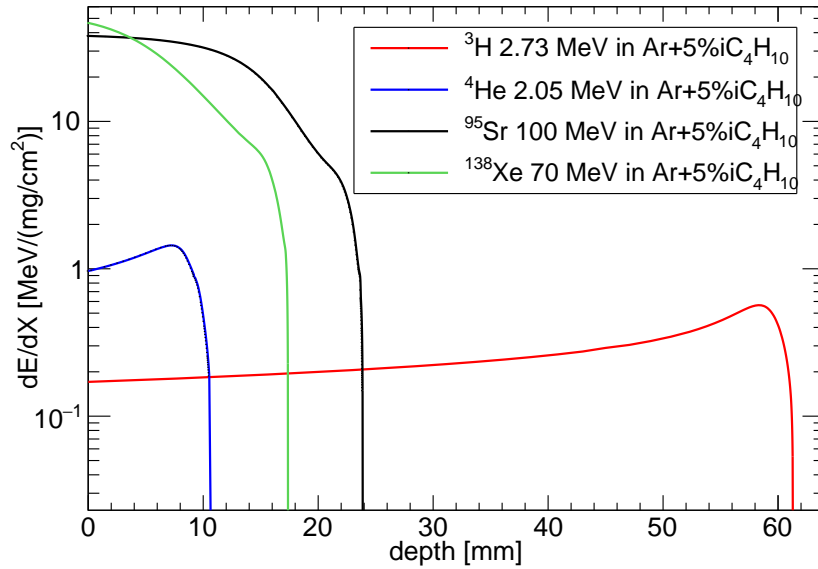


Figure 4. The Bragg curve calculated from SRIM data for an alpha, a triton, and for two typical fission fragments ^{95}Sr and ^{138}Xe .

where the simulated energy deposition histogram (left plot) is presented as well as the energy deposition spectra for different drift gaps. For the current study, a drift gap of 1 cm is chosen. Using the FLAIR graphical interface for FLUKA [15], the fluence of alphas and tritons can be plotted, expressed in particles/cm²/primary, as it can be seen in figure 6. As expected, alpha particles have a shorter range than the tritons due to their larger energy loss per unit path length. Thus, alpha particles emitted in forward directions have on average lost less energy in the ^6LiF layer and have longer tracks than those emitted under larger angles (figure 6 – left plot). As a result, the energy deposition of the alpha tracks is recorded by a few strips within 1 cm around the point of interaction of the neutron beam with the ^6LiF layer and corresponds to the high right peak of the simulated total amplitude distribution (figure 5 – left plot). On the contrary, the tritons deposit little energy along their track and thus have longer tracks that could extend to the edges of the detector (figure 6 – right plot) and form the two lower peaks/bumps of the simulated total amplitude histogram (figure 5 – left plot).

In figure 7, the scoring of the plain double differential yield of triton/alpha particles is shown, as a function of the polar angle (degrees) with respect to the beam direction, in the boundary surface between ^6LiF and gas (left plot) or gas and copper end plate (right plot), from 0 to 90 degrees in 10 bins, and in one interval covering the full energy range (the USRYIELD FLUKA estimator is used that scores the double differential yield of particles escaping from a surface). The differential yield always refers to the solid angle in steradian, even if the x-axis is specified as the polar angle in degrees. The results indicate that alphas and tritons entering in the gas from the ^6LiF converter, have both the same yield in all angular bins with the exception of angles $> 80^\circ$ where practically the alphas can not get out from the converter. In case of the copper end plate of the detector, the yield of both particles is similar for angles up to 30° , then the yield of tritons is constant up to 70° and subsequently drops, while in case of alphas is decreasing and practically approaching zero at angles $> 60^\circ$, since the alphas emitted at large angles cannot reach the copper end plate. In order to get more information and visualize the tracks in a 3D representation, the "MGDRAW" FLUKA subroutine is evoked as a general event interface that enables us to record the track segments of alphas and tritons in the gas for all

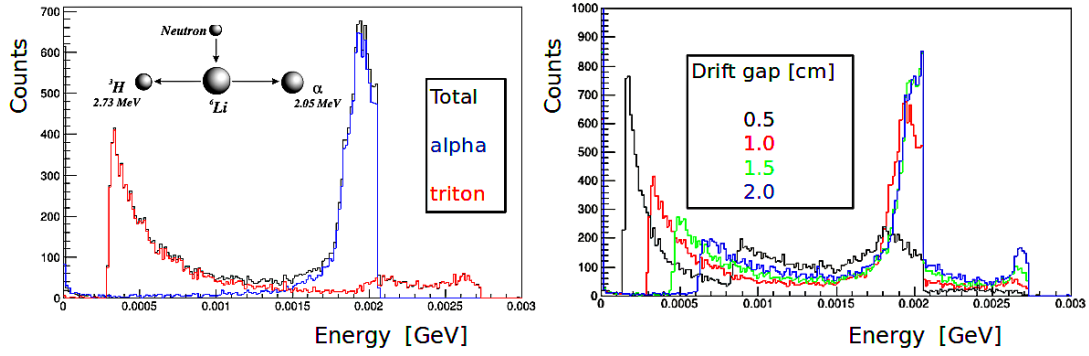


Figure 5. The simulated energy deposition spectra in the gas (black line) resulting from the response of the detector to thermal neutrons using a ${}^6\text{LiF}$ converter where the alpha particle (blue curve) and the triton (red curve) contribution are shown (left plot) as well as the total energy deposition in the active gas as a function of the drift gap up to 2.0 cm (right plot), based on FLUKA.

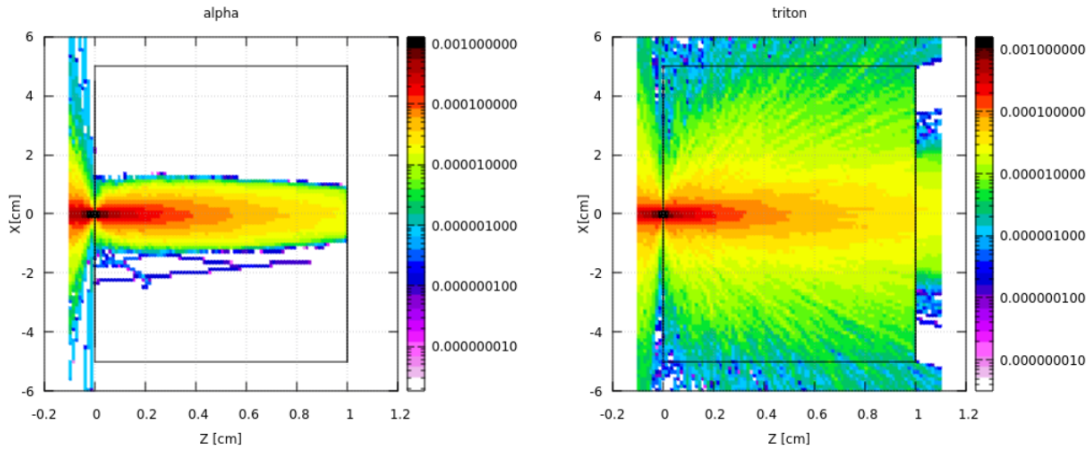


Figure 6. The simulated particle fluence by FLUKA (track-length density expressed in particles/cm²/primary) for alpha (left plot) and triton (right plot) particles emitted with energies ~ 2 MeV and ~ 2.7 MeV respectively from the ${}^6\text{LiF}$ layer at $Z = 0$. The solid black lines determine the borders of the active gas volume.

continuous energy deposition events. In figure 8, the distributions of the energy deposition in the X, Y, Z coordinates of the alpha (left) and triton (right) in the active gas volume with a number of continuous energy deposition events along each track are shown.

Then, by applying a selection of criteria at the track level, the simulated total amplitude spectra can be cleaned out. Thus, the condition " $|x, y_{track}| < 2$ cm", is actually equivalent with the recording of the deposition events by a few strips within 2 cm around the point of interaction of the neutron beam with the ${}^6\text{LiF}$ layer. With the aforementioned condition, the lower peaks/bumps on the right of the raw energy deposition histogram are removed, proving that their origin are tritons that are emitted at large angles (figure 9 – left plot). In addition, requiring " $z_{track} > 1$ cm", only tracks that terminate in the copper end plate of the "XY" micromegas detector are recorded (figure 9 – right plot). The use of FLUKA or Geant4MC code for the estimation of the energy deposition in the gas is expected to reproduce quite well the experimental total amplitude distributions. But the full tracking of all secondary electrons that are created by ionization and recording their "end" positions due to the applied voltages on the

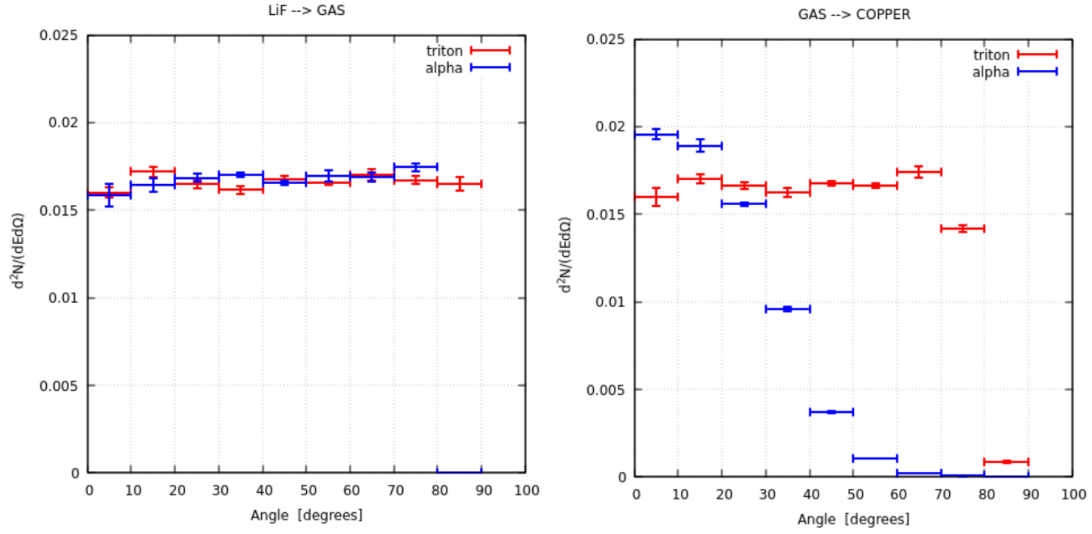


Figure 7. Distribution of the double-differential particle yield for triton (red points) and alpha (blue points) across a boundary surface from ${}^6\text{LiF}$ to gas (left plot) and from gas to copper end plate (right plot). Angles with respect of the beam direction (polar angles in degrees) and results normalized as double differential, expressed in $[\text{particles GeV}^{-1}\text{sr}^{-1}/\text{primary}]$, based on FLUKA simulations.

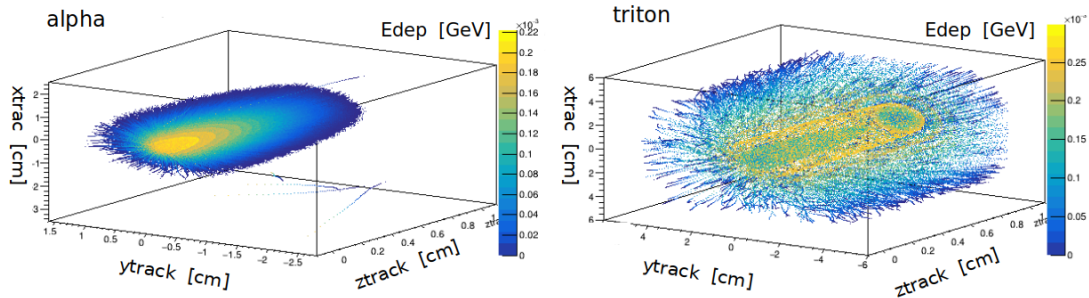


Figure 8. Distribution of the energy deposition in the X, Y, Z coordinates of the alpha (left) and triton (right) in the active gas volume with a number of continuous energy deposition events along the track based on FLUKA, where $xtrack$, $ytrack$, and $ztrack$ are given in cm and the energy deposition (E_{dep}) in GeV.

top and bottom side of the gas volume is not possible so far.

Therefore, a dedicated study using Garfield++ [9] (an object-oriented toolkit for the detailed simulation of particle detectors based on ionisation measurement in gases) is required, following and extending the work that is reported in ref. [16]. The main aim of this work is to fully reproduce the expected experimental results using this code and compare them with the ones obtained by the FLUKA MC code. The simplified geometry as shown in figure 1, is implemented in Garfield++ and the respective values of the applied voltages HV3 (V_{drift}), HV2 (V_{mesh}), HV1 (V_{pad}) were -600 V, 0 V and +350 V respectively. The modelling of the electric fields in the drift gap and amplification gap is done using two separate Component Analytic Field objects, each with a parallel-plate configuration.

At first, the appropriate gas file for electron transport is required to be produced, using the Magboltz program that is a part of the Garfield++ code. Thus, a table of transport parameters

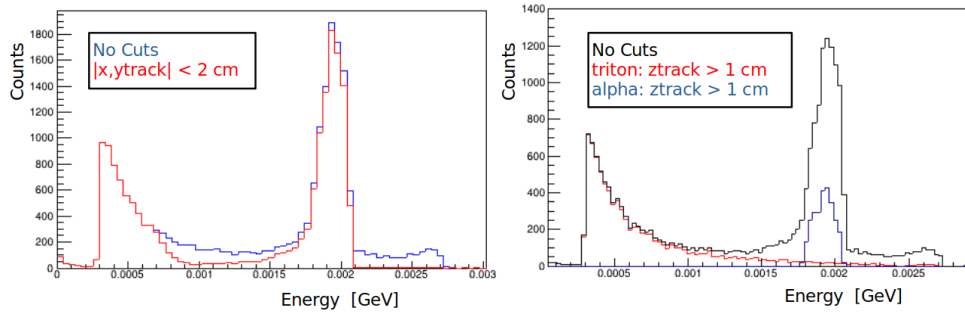


Figure 9. Monte Carlo simulation results based on FLUKA where the application of cuts at the track level requiring $|x, y_{track}| < 2$ cm and $z_{track} > 1$ cm, of a perpendicular pencil-like thermal neutron beam hitting the ${}^6\text{LiF}$ layer.

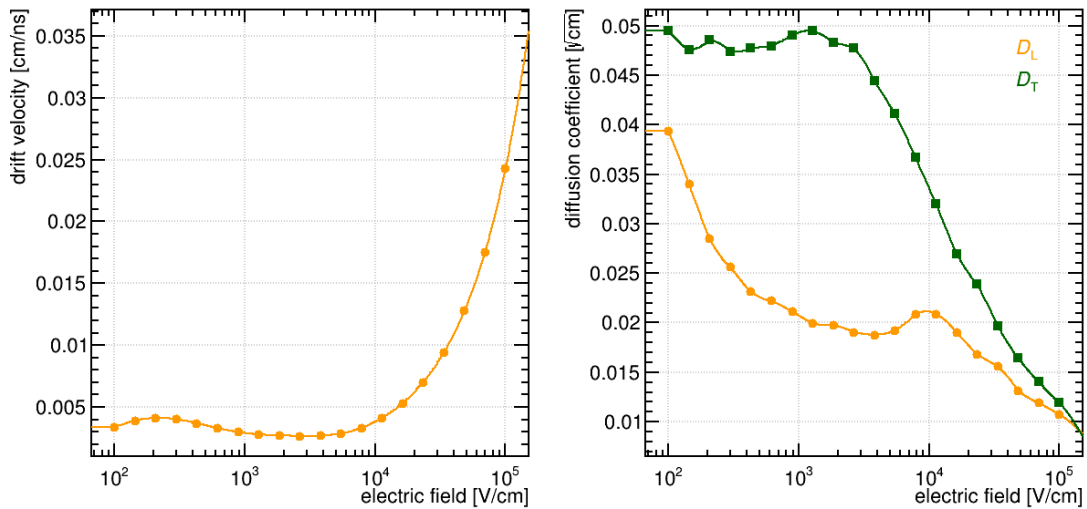


Figure 10. Drift velocity and diffusion coefficients (transverse and longitudinal diffusion coefficients) for a gas mixture of Ar- $i\text{C}_4\text{H}_{10}$ (5%) at NTP as calculated by Magboltz.

is prepared (drift velocity, diffusion coefficients, Townsend coefficient and attachment coefficient) as a function of the electric field E , for a gas mixture of 95% argon–5% isobutane at a pressure of 1 atm and room temperature. The drift velocity and the diffusion coefficients as calculated by Magboltz are shown in figure 10.

The alpha or the triton particle heavily ionizes the gas and the electric field drifts the secondary electrons to the micromesh which is then scored as charge, representing real-life parallel plate detectors. The drift lines of the electrons created along the track are calculated using the Runge-Kutta-Fehlberg (RKF) integration method, implemented in the class `DriftLineRKF`. This method uses the previously computed tables of transport parameters to calculate drift lines and multiplication. An other more detailed but very time consuming method that is also used is the microscopic tracking method that is implemented in the class `AvalancheMicroscopic` (written as MC in most of the plots), where the electron is followed from collision to collision. The α particle will produce a large number of electron/ion pairs in the gas so it's probably an overkill to use `AvalancheMicroscopic` because most of the fluctuations will be washed out. With `DriftLineRKF` there is no random/Monte Carlo element in the drift line simulation. For a given starting point, all electrons/ions will go at the same end point. On the other hand, microscopic tracking of electrons is typically used when fluctuations are important (for instance, when an

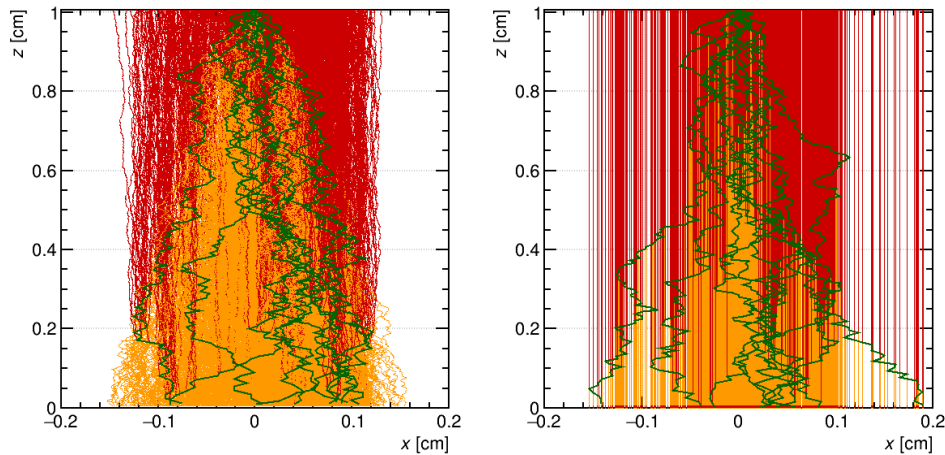


Figure 11. 2D x-z projection of 10 alpha vertical tracks with energy of 2 MeV with MC microscopic tracking of electrons (left plot) and drifting of electrons using the RKF integration method (right plot) where in green are the alpha tracks, in orange the electron tracks and in red the ion tracks.

accurate description of diffusion is needed, especially in non-uniform fields, or for studies of gain fluctuations in the avalanche gap to get the ion signal). For the electrons in the drift gap, diffusion will just spread the arrival points of the electrons at the mesh. In this case, we are looking at the signal induced on the mesh plane as a whole. Both methods are used and compared with each-other. Figure 11 illustrates in a 2D X-Z projection the tracks of 10 vertical α particles of 2 MeV using the MC microscopic tracking of electrons (left plot) and the RKF integration method (right plot). It should be noted that in the plot where the MC method was used, only the drift lines of the primary electrons are shown because the very large number of secondary electrons did not allow to make a useful plot. This study was carried out as follows: Initially, we generated vertical 2 MeV α -particles and 2.7 MeV tritons with Garfield++ and we collected simulated data for the deposited charge in the anode electrode (pad) using the RKF method. The information for the energy loss for both ionizing particles is obtained by using the SRIM code (version: SRIM-2013.00) [10] and producing outputs with stopping units expressed in MeV/(mg/cm²). It is also essential to load a file with the mobility of the ions in argon that can be found in the installation folder of Garfield++. Then, retrieving the "clusters" along the track, the drift is simulated for each of the primary electrons. The drift lines of the electrons released in the drift gap will stop once they hit the mesh plane. After putting together the code, the result of the simulation of the drift of the electrons looks something like the image below in figure 12.

It is important to note that for the creation of one pair of electron—ion an energy $W = 26$ eV (work function for argon) is needed. Thus, a 2 MeV α -particle could create up to $(2 \text{ MeV} / 26 \text{ eV}) \sim 75\text{K}$ pairs. Taking into account the geometry of the detector, the expected pulse height is ~ 1.4 mV without any amplification yet. The ratio of time needed for a single alpha track to be simulated using the RKF method as compared to the microscopic MC method is about 1 to 4000. In the same manner, the drift of the electrons generated along the track was simulated using the microscopic tracking method in order to evaluate the spread of the arrival points of the electrons in the mesh and estimate the magnitude of the diffusion. In order to compare the results from the two methods, 200 vertical tracks of 2 MeV α -particles and 2.7 MeV tritons were tested.

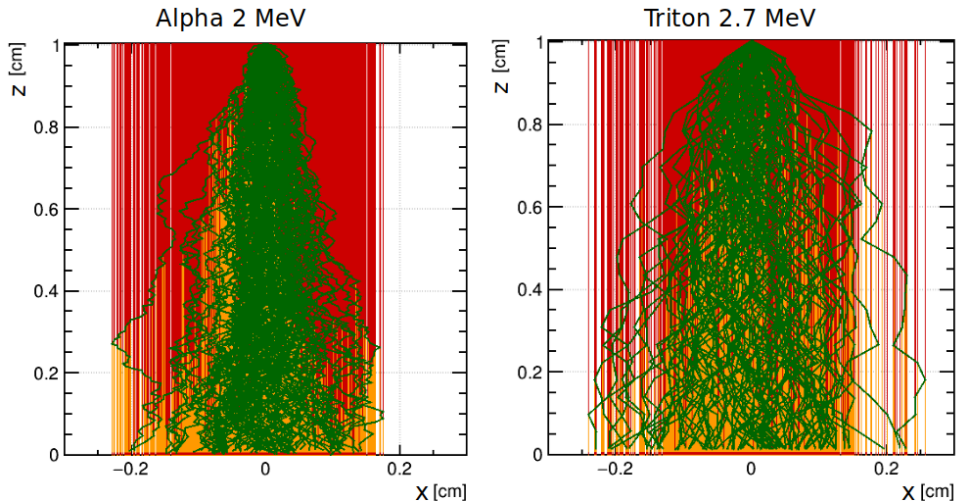


Figure 12. 2D x-z projection of 100 alpha and triton vertical tracks with energies of 2 and 2.7 MeV with the RKF drift line method.

Both methods produce the same number of primary electrons that are ~ 152 / alpha track and ~ 24 / triton track, while the secondary electrons produced by the microscopic MC method are ~ 75.3 K / alpha track and ~ 11.6 K / triton track that are tracked up to the mesh where they terminate, that are in perfect agreement with the expected quantities of electron—ion pairs. The results of the microscopic MC method, indicate that the standard deviations of the distributions of the arrival positions in the XY end plane of the primary electrons as well as of all electrons (if the secondaries are tracked as well), are almost equal. That could enable us using the MC method but tracking only the primary electrons without the tracking of the secondaries that require enormous time. Therefore, 10000 alpha and triton vertical tracks were tested with both methods. The 2D distributions of the arrival positions of the electrons plotted in a binning of [0.01 cm / bin] in the XY plane, using the RKF method are shown in figure 13.

The respective 2D distributions of the arrival positions of the primary electrons using the microscopic MC method are presented in figure 13 as well, without and with diffusion. The following Table 1 illustrates the results of the Garfield++ simulations based on the two aforementioned methods. A comparison of the standard deviations presented, indicates that the RKF method and the microscopic MC model give equivalent results in case we extract from the latter the initial positions of the primary electrons that actually provide the spread of the electrons in the XY plane without diffusion. From the same run with the microscopic MC model, the final positions of the primary electrons are recorded as well, giving the actual spread of the electrons due to diffusion. Therefore, a single run using the microscopic MC model, enabling only the tracking of the primary electrons, could provide all information needed for assessing the effect of diffusion. Taking into account that the active area of the current detector prototype is 10×10 cm², divided into 100 + 100 strips with 1 mm width, the effect of diffusion should be considered rather negligible for vertical tracks.

In the second step, for a specific vertical trajectory, the integral of the induced current pulse related to the total induced charge is obtained, without any convolution yet with a transfer function, in the mesh and in the pad, using the class IntegrateSignals and can be seen in figure 14. The obtained signal out of one single track using the RKF drift line method results at a deposited charge (given by the total number of electrons arrive at the mesh multiplied by the elementary charge) of 12.1 fC for an alpha and 1.9 fC for a triton. With q_{drift} and q_{pad} defined as

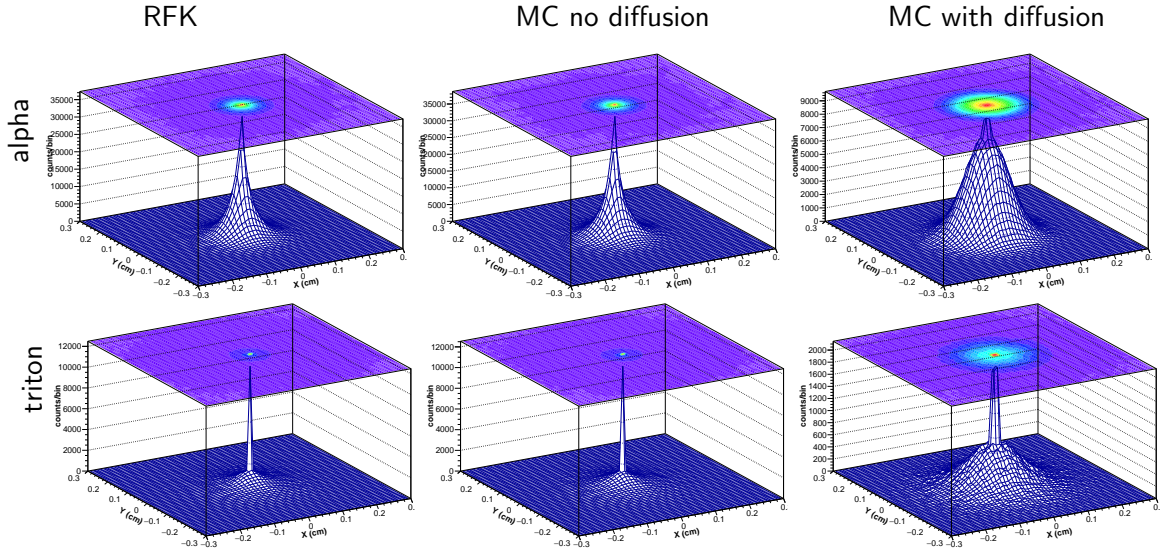


Figure 13. 2D distributions of the arrival positions of the electrons plotted in a binning of [0.01 cm / bin] in X and Y, for 10000 vertical tracks of alphas (upper 3 panels) and tritons (lower 3 panels), using from left to right the RKF method, and the microscopic MC method enabling only the tracking of primary electrons, without and with diffusion of the electrons.

Table 1. The standard deviations of the 2D distributions of the arrival positions of the primary electrons that are produced from 10000 vertical alpha / triton tracks with RKF and MC methods.

| Method | RKF | MC no diffusion | MC with diffusion |
|-------------------------------|------|-----------------|-------------------|
| σ_{alpha} (mm) | 0.46 | 0.46 | 0.57 |
| σ_{triton} (mm) | 0.70 | 0.70 | 0.77 |

the charges deposited on the micromesh (end of drift region) and on the anode respectively, $q_{\text{drift}} = 6.1$ fC and $q_{\text{pad}} = -6.8$ pC for alphas and 0.9 fC and -1.0 pC for tritons. Using an approximate GET transfer function with a shape shown in figure 15 [17] and the class ConvoluteSignals, the expected pulse from alpha/triton tracks inclined at 45 degrees is illustrated in figure 16. This pulse should be inverted in y-axis to be compatible with the electronics used at CERN that usually require negative pulses as a primary input. The pulse height distribution data extracted per track provides the distribution of the energy deposited.

The final part of the analysis was to generate a simulated spectrum of α -particle and triton tracks as exited from the ${}^6\text{LiF}$ target, having trajectories distributed within the whole detector volume, using Garfield++ and then to compare it qualitatively with the simulated total energy deposition histogram as calculated by FLUKA. The energies of the ionizing particles are the ones evaluated by FLUKA from ${}^6\text{LiF}$ target to the gas using a boundary crossing estimator as a part of the MGDRAW subroutine (that enables us also to record the direction cosines of alpha and tritons in the boundary) and can be seen in figure 17. The 2D X-Y projection of 1000 alpha and triton tracks inside the gas, with kinetic energy and initial direction calculated by FLUKA, is shown in figure 18 which looks alike the figure 6. At the left of figure 19 is the simulated energy deposition spectrum by FLUKA MC and at the right is the deposited charged on the mesh (multiplying the total number of electrons per track with the elementary charge) for the same number/type of tracks as calculated by Garfield++ using the RKF method. The qualitative similarities between those two spectra are very encouraging indicating the linear response of the

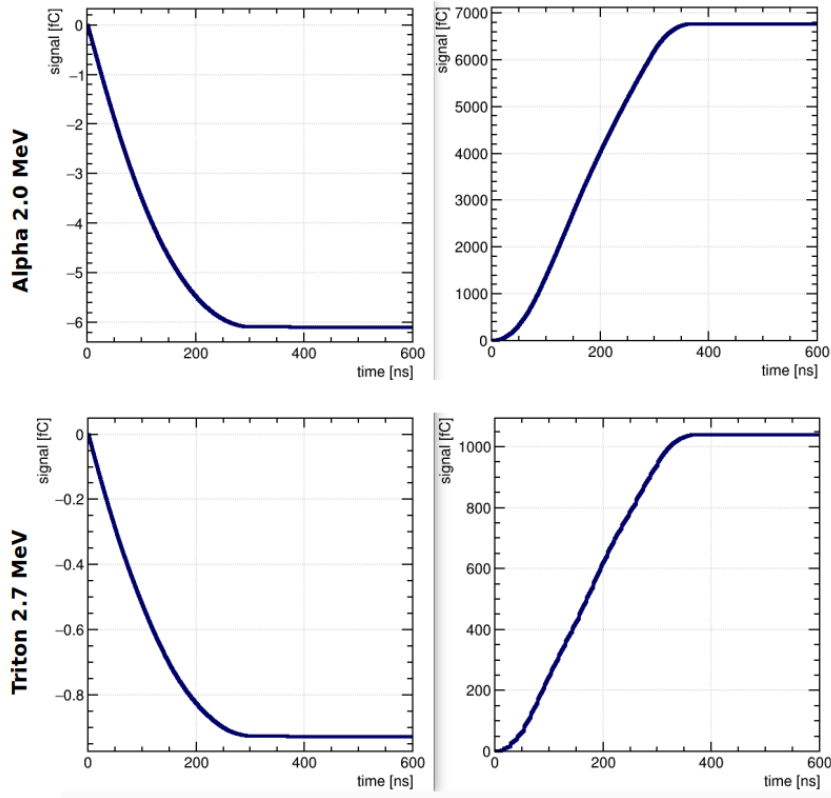


Figure 14. The integral of the induced current pulse related to the total induced charge without any convolution yet with a transfer function for a single vertical alpha / triton track on the drift (left) and on the pad (right).

detector.

Following this scheme of analysis, we plan to address and carry out studies using other type of converters that evoke $^{10}\text{B}(n,\alpha)$ reactions and also fission fragments. The proposed method is to extract at first with a transport MC code (FLUKA, Geant4) the energies and direction cosines of the neutron reaction products and then use Garfield++ to transport them in the drift region and record all the primary electrons that arrive on the micromesh, using the full MC microscopic model enabling only the tracking of primary electrons.

4 Conclusions

The work performed for this part of deliverable D1.1 concerns extended simulations of a Micromegas XY detector with dedicated VMM3-chip electronics for the data acquisition, compatible with neutron time-of-flight measurements. The relative transparency of the detector to neutrons has opened up opportunities for layered experimental setups, including the stacking of similar detectors and the integration with downstream neutron-induced reaction measurements.

We have focused the simulation studies on a standard iron-55 X-ray source, and on the neutron to charged particle converters using the nuclei lithium-6 and boron-10 which have cross sections considered standard. Moreover, those nuclei can be used in a standard lab-environment. With Micromegas detectors the gain can be simply adjusted by the high voltage and adapted to the much higher energies of fission fragments from for example uranium-235.

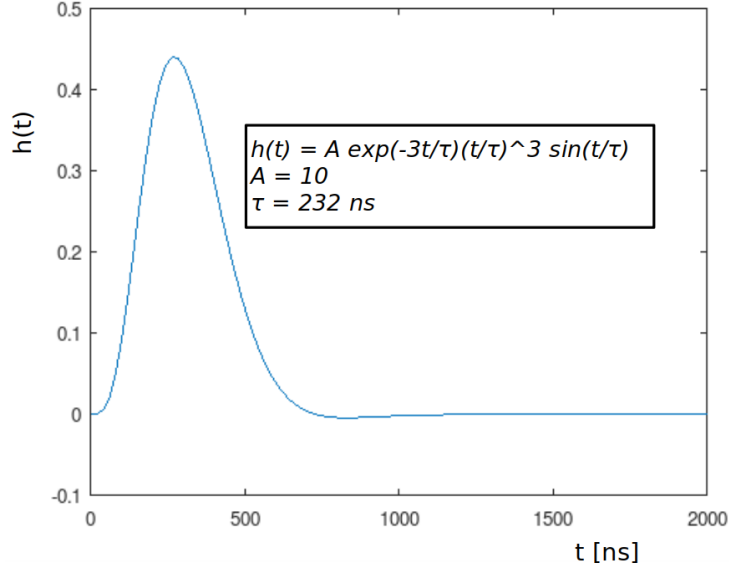


Figure 15. Transfer function used for the convolution of the signal.

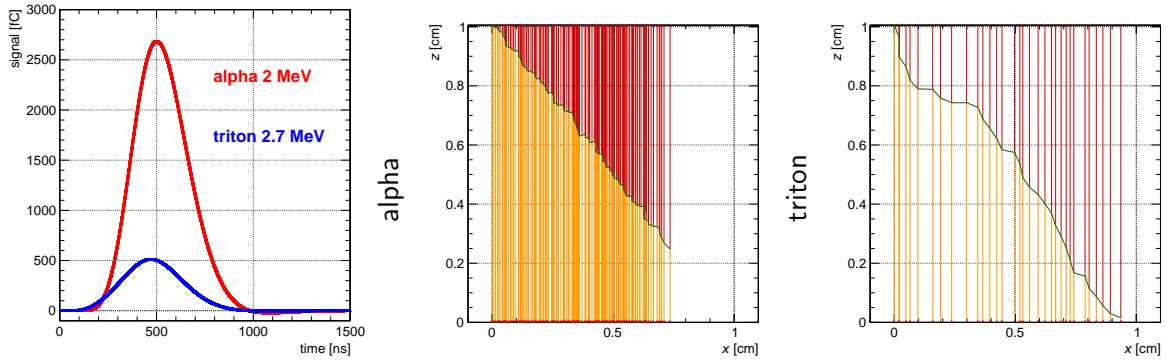


Figure 16. RKF convoluted q_{pad} (anode) signal that provides the pulse (left plot) for one alpha / triton track (middle and right plot) inclined at 45 degrees in a 2D x-z projection.

A solid simulation framework for this detector has been established using the current state-of-the-art Monte Carlo computer codes FLUKA, Geant4 and Garfield++, as well as the code SRIM giving access to a large collection of empirical gas properties. We have delved deeply into the subtleties of energy deposition of ionizing particles in the gas volume, and the subsequent electron transport and amplification in the electric fields of the detector. The simulations have provided crucial insights in the potential applications of the detector.

The presented work within the SANDA environment serves as a guiding framework for the construction of the next prototype of the detector which is part of a follow-up project funded by the French national funding agency ANR.

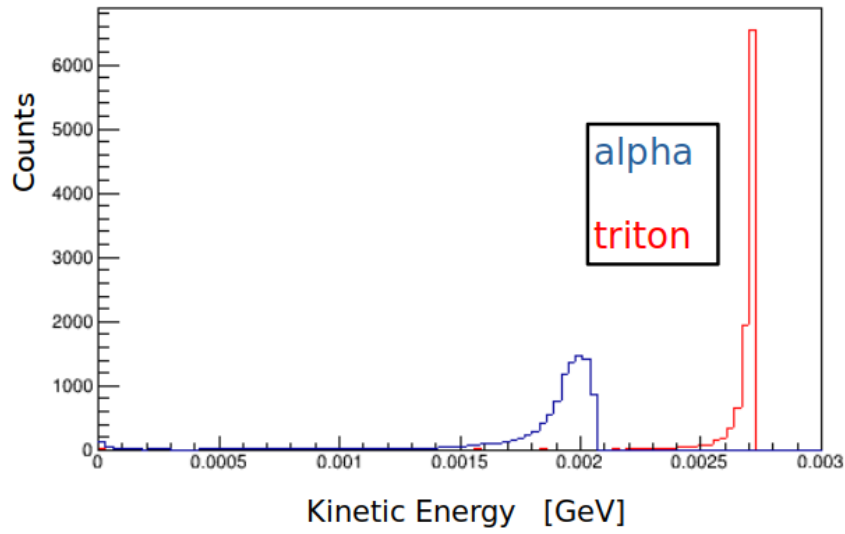


Figure 17. Kinetic energy of alpha and triton entering in the gas from the ${}^6\text{LiF}$ target, as calculated by FLUKA.

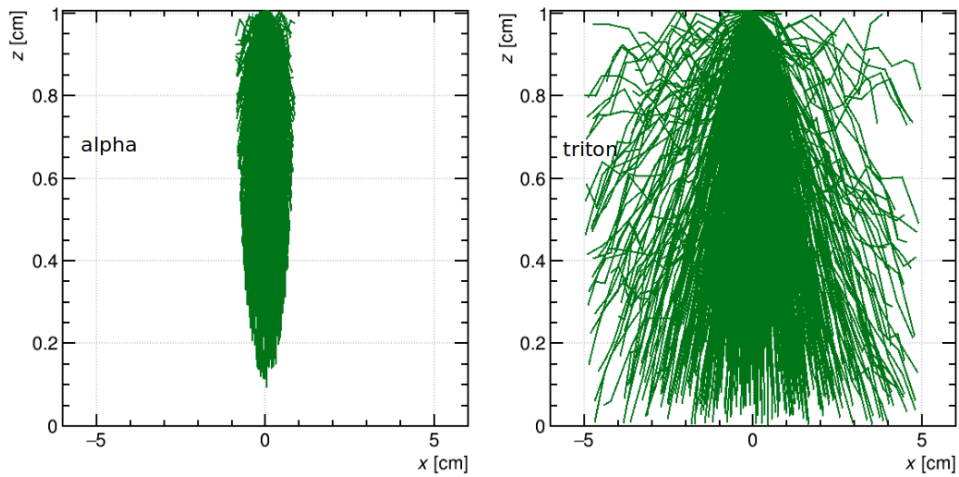


Figure 18. The 2D x-z projection of 1000 tracks of alpha (left plot) and triton (right plot) with kinetic energy and initial direction estimated by FLUKA.

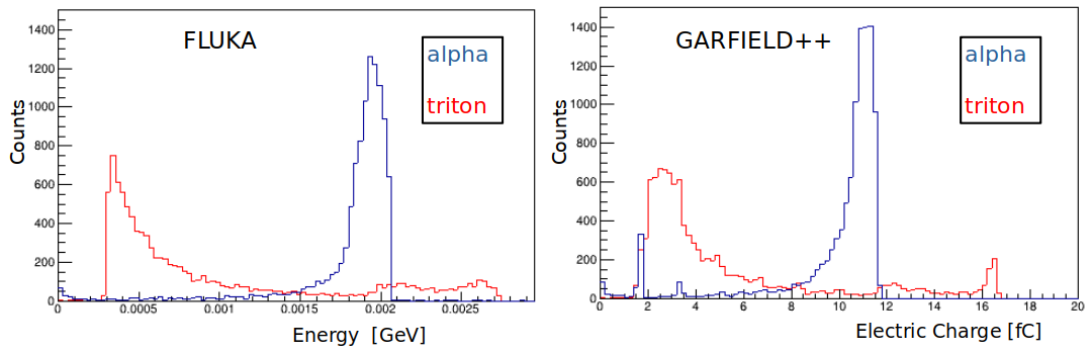


Figure 19. FLUKA energy deposition spectrum (left plot) and RKF deposited charge (right plot) in the active gas volume for ~ 10000 alpha / triton tracks with kinetic energy and initial direction estimated by FLUKA.

References

- [1] David Attié et al. Current status and future developments of micromegas detectors for physics and applications. *Applied Sciences*, 11(12):5362, 2021. doi:10.3390/app11125362.
- [2] F. Belloni et al. Micromegas for neutron detection and imaging. *Mod. Phys. Lett. A*, 28(13):1340023, 2013. doi:10.1142/s0217732313400233.
- [3] M. Diakaki et al. Development of a novel segmented mesh micromegas detector for neutron beam profiling. *Nucl. Instrum. Methods A*, 903:46–55, 2018. doi:10.1016/j.nima.2018.06.019.
- [4] A. Ferrari, P.R. Sala, A. Fasso, and J. Ranft. *FLUKA: A Multi-Particle Transport Code*. 2005. CERN-2005 10, INFN/TC_05/11, SLAC-R-773. doi:10.2172/877507.
- [5] T.T. Böhlen, F. Cerutti, M.P.W. Chin, A. Fassò, A. Ferrari, P.G. Ortega, A. Mairani, P.R. Sala, G. Smirnov, and V. Vlachoudis. The FLUKA code: Developments and challenges for high energy and medical applications. *Nuclear Data Sheets*, 120:211–214, June 2014. doi:10.1016/j.nds.2014.07.049.
- [6] A. Fasso, A. Ferrari, G. Smirnov, F. Sommerer, and V. Vlachoudis. FLUKA realistic modeling of radiation induced damage. *Progr. Nucl. Science and Technology*, 2(0):769–775, 2011. doi:10.15669/pnst.2.769.
- [7] S. Agostinelli et al. Geant4 - a simulation toolkit. *Nucl. Instrum. Methods A*, 506(3):250–303, jul 2003. doi:10.1016/s0168-9002(03)01368-8.
- [8] J. Allison et al. Recent developments in Geant4. *Nucl. Instrum. Methods A*, 835:186–225, 2016. doi:10.1016/j.nima.2016.06.125.
- [9] Garfield++. URL: <https://garfieldpp.web.cern.ch/garfieldpp/>.
- [10] J. F. Ziegler et al. SRIM – the stopping and range of ions in matter (2010). *Nucl. Instrum. Methods B*, 268(11–12):1818–1823, 2010. doi:10.1016/j.nimb.2010.02.091.
- [11] D.S. McGregor et al. Design considerations for thin film coated semiconductor thermal neutron detectors—I: basics regarding alpha particle emitting neutron reactive films. *Nucl. Instrum. Methods A*, 500(1–3):272–308, 2003. doi:10.1016/s0168-9002(02)02078-8.
- [12] D.S. McGregor et al. Thin-film-coated bulk GaAs detectors for thermal and fast neutron measurements. *Nucl. Instrum. Methods A*, 466(1):126–141, 2001. doi:10.1016/s0168-9002(01)00835-x.
- [13] Iaea stopping power data. URL: <https://nds.iaea.org/stopping>.
- [14] The ASTAR program, stopping power and range tables for helium ions. URL: <https://physics.nist.gov/PhysRefData/Star/Text/ASTAR.html>.
- [15] V. Vlachoudis. Flair website. URL: <https://flair.web.cern.ch/flair/>.
- [16] Marios Davis, Maria Diakaki, Michael Kokkoris, Veatriki Michalopoulou-Petropoulou, and Roza Vlastou. Simulation of a micromegas detector for low-energy α -particle tracking using garfield++. *HNPS Advances in Nuclear Physics*, 28:251–256, 2022. doi:10.12681/hnps.3715.
- [17] J. Giovinazzo et al. Get electronics samples data analysis. *Nucl. Instrum. Methods A*, 840:15–27, 2016. doi:10.1016/j.nima.2016.09.018.